Subproject F1.02

Electronic and Morphological Properties of Organic and Hybrid Solar Cells

Principle Investigators: Uli Lemmer and Dagmar Gerthsen

CFN-Financed Scientists: Daniel Weissenberger (1/2 E13, 2 months), Jan Brückner (1/1 E13, 9 months), Marina Pfaff (1/2 E13, 10.5 months), Philipp Müller (1/2 E13 since 1.10.2010)

Further Scientists: Dr. Alexander Colsmann, Michael F.G. Klein, Manuel Reinhard, Andreas Pütz

Lichttechnisches Institut
KIT

Laboratorium für Elektronenmikroskopie
KIT

Not for publication on the CFN-homepage (contains unpublished results)

Electronic and Morphological Properties of Organic and Hybrid Solar Cells

Introduction and Summary

Due to their potential for low cost photovoltaic applications, polymer solar cells have attracted a lot of attention over the last decade. In rapid succession of the first reports on bulk-heterojunction (BHJ) based organic solar cells (OSCs) comprising solution processable blends of semi-conducting polymers and fullerenes as the active layers in the 1990s [1], great efforts have been made to improve the performance of these blend systems. The main challenges to be solved in order to enhance photovoltaic performance are an insufficient spectral coverage of the solar spectrum, non-optimized cell architectures and poor control of the nanoscale morphology [2]. By careful consideration of these effects OSCs with power conversion efficiencies exceeding 7 % have been fabricated [3,4].

Upon deposition of the blend, an interpenetrating network of polymers and fullerenes is established. Photons absorbed by the polymer generate excitons that diffuse to the polymer/fullerene interface. There, the electron is transferred to an energetically more favourable fullerene domain. Since the exciton diffusion length in organic semiconductors is typically in the order of less than 15 nm [5], domain sizes should be in the same order of magnitude for reasonable exciton dissociation. In order to collect these charge carriers at the contacts percolation paths through the respective domains to the electrodes must be provided [6]. Thus, an optimized nanoscale morphology has to provide sufficient internal interfaces and contiguous transport paths at the same time.

On the microscopic level the morphology depends on the tendency of the organic molecules to self-assemble and crystallize during deposition. The nanoscale morphology of the active layer can be influenced by changing the process conditions, e.g. the choice of the solvent [7,8], the variation of the deposition temperature, the control of the drying kinetics [F1.2:7] and thermal post-treatment [9,10].

Typically, atomic force microscopy (AFM) imaging is used to analyze the surface of the active layer [11] while transmission electron microscopy (TEM) is carried out to probe the volume of a thin sample [6]. However, TEM analysis is hampered by limitations such as electron knock-on damage [12], and especially poor contrast for samples containing materials that consist of light elements with only small variations in density. On the other side, the nanoscale morphology changes on the macroscopic optoelectronic properties can be analyzed e.g. by means of UV-VIS absorption spectroscopy or electro-optical measurements such as current density/voltage (JV) and external quantum efficiency measurements [6].

We have investigated blends of poly(3-hexylselenophene-2,5-diyl) and [6,6]-Phenyl C_{61}-butyric acid methyl ester (P3HS:PCBM). P3HS is the selenium equivalent of the well studied poly(3-hexylthiophene-2,5-diyl) (P3HT), exhibiting a reduced optical band gap due to a deeper lowest unoccupied molecular orbital (LUMO) energy level resulting from a smaller ionization potential of selenium compared to sulfur [2].

To overcome the problem of poor contrast between PCBM and P3HS in conventional TEM imaging, we apply here scanning transmission electron microscopy (STEM) at low electron energies < 30 keV using a high-angle annular dark-field (HAADF) detector. Among the different STEM imaging modes, the HAADF mode is particularly useful because composition-sensitive (Z-) contrast can be obtained which allows to image sensitively compositional inhomogenities on a small spatial scale [13-15]. Lowering the electron energy E intrinsically leads to an improved Z-contrast [16]. An experimental verification was presented already for thin carbon films which shows contrast enhancement by one order of magnitude after reduction of E from 100 keV to 15 keV [17]. Despite of the high chemical sensitivity of HAADF STEM at low electron energies, few

applications of this technique were presented up to now. Within this project we have shown, that low-energy (low-keV) HAADF STEM is well suited to image the distribution of PCBM and P3HS which differ only slightly in average atomic number and density. In order to analyze spatial structures and in particular domain sizes quantitatively, we utilize spatial Fourier transform. We compare low-keV STEM micrographs of as-deposited and thermally annealed OSCs incorporating P3HS. Annealing leads to the formation P3HS whiskers. This in turn leads to a red shifted optical absorption and an enhanced mobility as evidenced in the transient photoresponse.
In addition, we have carried out a methodological study on low-keV HAADF STEM imaging by comparing quantitatively experimental and simulated image intensities of different carbon-based materials [F1.2:11]. In the course of this study we have also evaluated different scattering cross sections which are used in Monte-Carlo (MC) image simulation. The potential of the technique is shown for measuring the local sample thickness.

Summary: The conjugated polymer poly-(3-hexylselenophene-2,5-diyl) (P3HS) is a promising donor material for organic solar cells as its absorption covers a large part of the visible spectrum up to 750 nm. We investigate bulk heterojunctions of P3HS and the fullerene derivative [6,6]-Phenyl C_{61}-butyric acid methyl ester (PCBM) as the active layer in organic photovoltaic devices. Annealing of the respective samples leads to the formation of needle-like structures that we identify as P3HS whiskers by means of low-energy scanning transmission electron microscopy utilizing a high-angle annular dark-field detector. A quantitative description of the size of the nanostructures was elaborated by means of spatial Fourier analyses. The results of electron microscopic studies are correlated with the macroscopic optoelectronic device properties, i.e. solar cell performance parameters, changes in the absorption spectrum and the impact on the time-dependent device photoresponse.

2. Low-keV STEM imaging of polymers and carbon-based materials

HAADF STEM at low electron energies of 30 keV and below is a promising technique for the analysis of light materials. Low-keV STEM images can be taken in a standard scanning electron microscope, which is equipped with a STEM detector (see scheme in **figure 1**). Using thin samples a high lateral resolution in the order of 1 nm can be achieved. Moreover, knock-on damage is almost completely avoided at low electron energies.

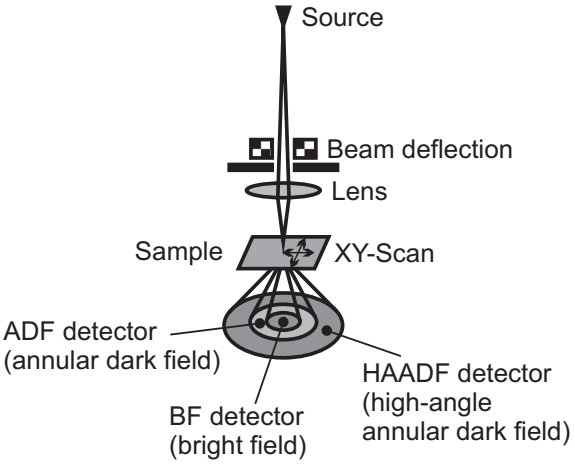

Figure 1. *Scheme of STEM in combination with a concentric detector array. While the bright field (BF) detector is located in the center, the annular dark-field (ADF) and the high-angle annular dark-field (HAADF) detectors collect electrons at higher angles.*

Since the intensity of HAADF STEM images is influenced by a set of parameters, an intuitive analysis in terms of Z-contrast is in general not possible. Therefore an adequate description of low-energy electron scattering in light materials is required. Several semiempirical equations were suggested which describe electron scattering for heavier materials and higher electron energies [18], which were analyzed if they are also applicable for light carbon-based materials and energies below 30 keV. For this purpose, we investigated low-energy electron scattering in amorphous carbon, P3HT (poly(3-hexylthiophene-2,5-diyl)) and EPON (epoxy resin) by HAADF STEM using samples with well-known thickness [F1.2:11]. Intensity line profiles of samples with a wedge-shaped thickness profile demonstrate, that the HAADF STEM intensity shows a characteristic maximum depending on the sample thickness, material parameters and electron energy (**figure 2**).

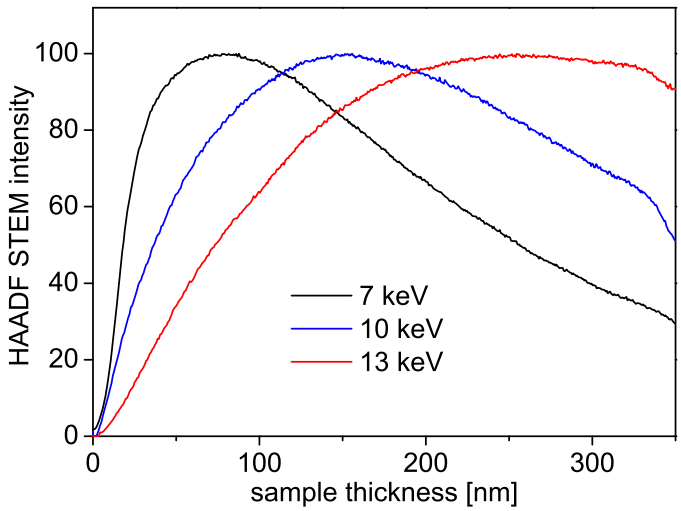

***Figure 2**. normalized HAADF STEM image intensity of a wedge-shaped carbon sample as a function of the local sample thickness at 7, 10 and 13 keV.*
The intensity shows a characteristic maximum depending on the electron energy

At maximum HAADF STEM intensity, the sample thickness is a quadratic function of the electron energy. The experimental data was compared with existing semiempirical equations for electron scattering and an optimum fit of the experimental data was achieved on the basis of a semiempirical expression for the mean quadratic scattering angle $\overline{\theta_B^2}$ suggested by Bothe [19] with a modified correction factor of 9.15 instead of 12.94 as originally suggested:

$$\overline{\theta_B^2} = 9.15 \cdot 10^9 \left(\frac{Z}{E}\right)^2 \frac{\rho t}{A}$$

The electron energy E is given in eV and the mass thickness ρt in kg/m². Z is the atomic number and A the atomic mass number. The mean scattering angle can now be used to calculate the HAADF intensity:

$$I_{HAADF} = e^{-\theta_1^2/2\overline{\theta^2}} - e^{-\theta_2^2/2\overline{\theta^2}}$$

The angles θ_1 and θ_2 denote the minimal and maximal scattering angle covered by the HAADF STEM detector.
Figure 3 shows the calculated HAADF image intensity as a function of the electron energy for 150 nm thick P3HS and PCBM samples, which is the mean thickness of the examined absorber layers. At an electron energy of 9.5 keV contrast inversion occurs. Since this contrast inversion depends on the sample thickness, it is essential to calculate the image intensities before interpreting HAADF STEM images of P3HS:PCBM blends.

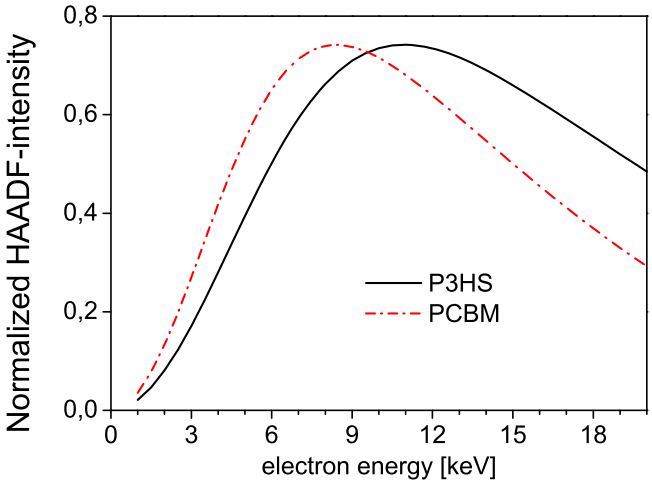

***Figure 3**. calculated HAADF STEM image intensity of 150 nm thick P3HS and PCBM samples as a function of the electron energy. The contrast is inverted at an electron energy of 9.5 keV.*

For the measurements shown in section 3, an electron energy of 15 keV was chosen to obtain optimum contrast between the two materials and a high intensity to obtain a good signal-to-noise-ratio.

3. Morphology of P3HS:PCBM bulk heterojunctions

The examined solar cells were produced by spincoating the heated P3HS:PCBM solution on poly(3,4-ethylenedioxythiophene):polystyrenesulfonate (PEDOT:PSS) covered ITO glass slides. During deposition we varied the temperature T of both, the solution and of the substrates between 70 °C and 100 °C simultaneously. Afterwards a calcium/aluminum electrode was evaporated.
After performing the electrical and optical characterization the active layers of the solar cells were peeled-off from the substrate and analyzed by low-keV STEM. To prepare electron-transparent samples we used a scalpel to cut the thin film between the electrodes of the solar cell into small pieces and dropped some water on it. As PEDOT:PSS is water soluble, small pieces of the active layer float off and can be picked up with conventional TEM grids.
In order to investigate the nano-morphology of the P3HS:PCBM thin films we use a FEI Strata400S dual-beam microscope with a STEM-HAADF detector. All images in this work were taken with a primary electron energy of 15 keV, a beam current of 0.58 nA and a frame time of 35.4 s. The electron beam diameter on the sample surface is on the nanometer scale which determines the optimum resolution of this technique. The resolution is reduced by beam broadening with increasing sample thickness. The contrast and brightness settings of the amplifier were adjusted to obtain comparable imaging conditions. As shown in section 2, the HAADF STEM intensity does not only depend on the chemical composition but also on the local sample thickness. This requires an analysis of possible sample thickness changes which need to be distinguished from compositional variations. Thus AFM measurements were performed utilizing an Anfatec Level AFM. The images were recorded in non-contact mode with a line speed of 0.5 lines per second.
By two-dimensional discrete spatial Fourier transform (2D-DFT) the STEM images were quantitatively analysed in the frequency domain and thereby information about the lateral phase separation within the blend was obtained. Since the spatial resolution Δ per pixel (here: 2.24 nm) was the same for both dimensions, an isotropic representation of the 2D-DFT was generated by averaging radially over all spatial frequencies [20,21].
As thermal treatment is well known to influence the nano-morphology of BHJs, we applied temperatures T between 70 °C and 100 °C to the solution and the substrate simultaneously upon deposition of the active layer. The low-keV HAADF STEM image of the as-spincast (T = 90 °C)

and non-annealed sample in figure 4a does not show any distinct features. After thermal treatment, however, the film morphology changes radically through the formation of needle-like structures (whiskers), exhibiting a high contrast as shown in **figure 4b**. Samples processed at 70 or 80 °C qualitatively show the same behavior after thermal post-treatment.

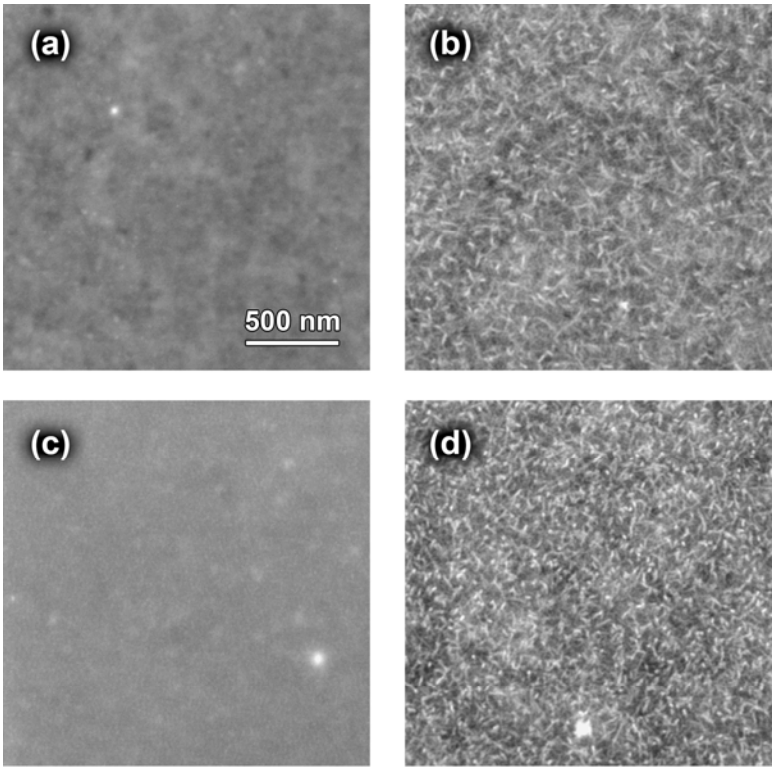

Figure 4. *Contrast enhanced low kV HAADF STEM images taken at 15 kV of 2 µm × 2 µm peeled-off P3HS:PCBM layers:*
(a) T = 90 °C, non-annealed,
(b) T = 90 °C, annealed, the annealed device exhibits needle-like P3HS structures,
(c) T = 100 °C, non-annealed,
(d) T = 100 °C, annealed,

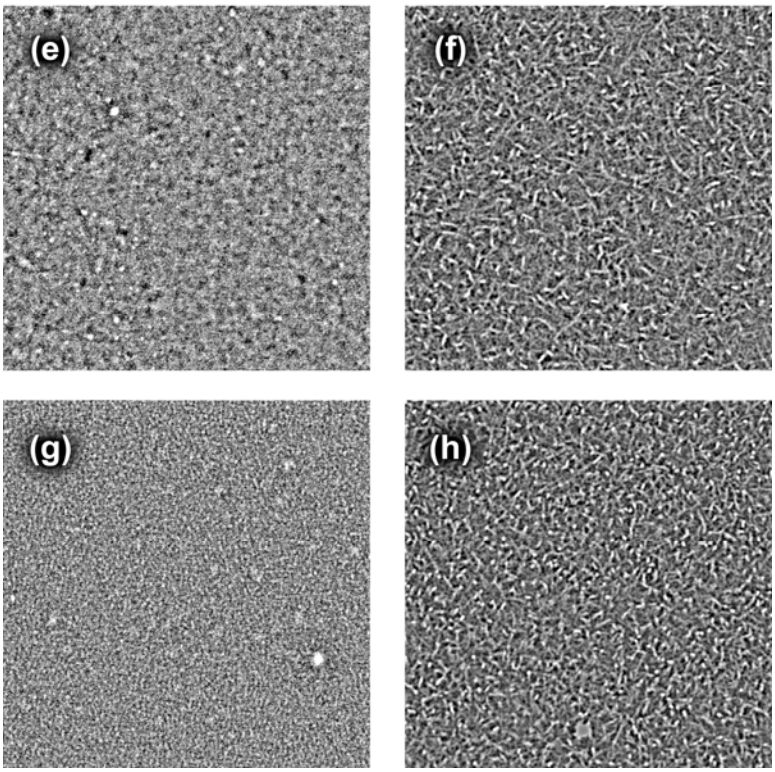

(e)-(h) first order Butterworth band-pass (8-80 nm) filtered images. First growth seeds of P3HS whiskers become visible in (g).

On the other hand, if the deposition temperature is only slightly increased to T = 100 °C or above, the as-spincast (non-annealed) layer in **figure 4c** already exhibits first weak features without any

thermal post-treatment. After thermal treatment the whisker density and characteristic shapes within these layers in **figure 4d** are comparable to the respective structures that become visible in the sample annealed at T = 90°C.
The predominant structure size within the P3HS:PCBM blend can be estimated from the isotropic representation of the 2D-DFT that was calculated from the respective low kV STEM micrographs. The results are depicted in **figure 5** where the logarithm of Fourier amplitude is plotted as a function of the logarithm of the spatial wavelength. The amplitude of the Fourier transform can be associated with the average lateral structure size and density within the blend [20,21]. The low Fourier amplitude in the lower spatial wavelength regime indicates the absence of structures at this length scale. However, the data at wavelengths well below 10 nm is affected by noise and resolution limitations and can thus not be analyzed.

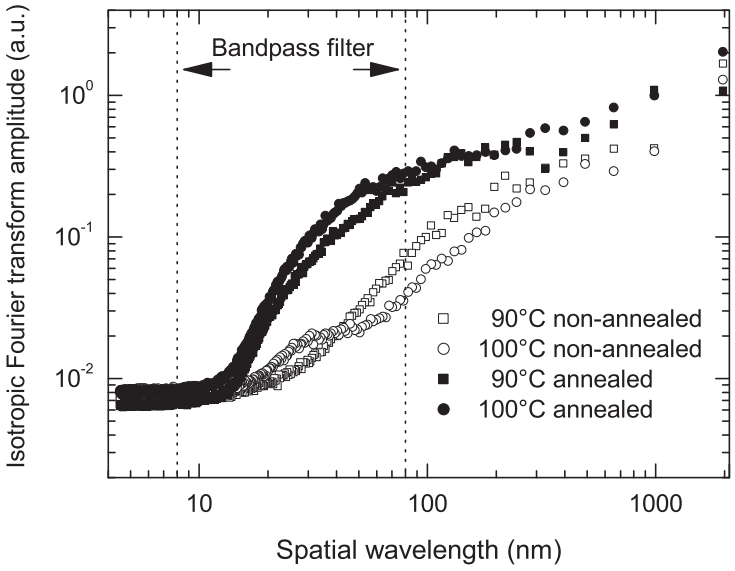

Figure 5. *Isotropic power spectral density of low-keV STEM micrographs of layers that were deposited at different temperatures T, before (open symbols) and after annealing (filled symbols). Smaller structure sizes become more prominent upon annealing and indicate whisker formation. At T = 100 °C or above smaller structures can be found in the non-annealed P3HS:PCBM layers (open circles) that we attribute to whisker seed formation. Dotted lines indicate bandpass filter cut-off wavelengths as applied to the images in figures 2 and 5.*

Comparing annealed and non-annealed samples we observe a significant increase of the Fourier amplitude for feature sizes between 15 nm and 300 nm after thermal treatment which can be correlated with the formation of structural features in this size interval. The smallest distinguishable structures after annealing are about 15 nm in size which is in good agreement with the width of the needle-like structures in the low kV STEM images (**figure 4**). The typical length of the needles corresponds to a few 10 nm up to about 100 nm. Comparing the samples before thermal treatment we observe an increase of the Fourier amplitude at about 30 nm for the layer deposited at 100 °C which indicates the beginning of the needle formation. On the contrary the sample deposited at 90 °C exhibits a higher Fourier amplitude in the range of about 50 nm up to 120 nm. These amplitudes represent larger structures like thickness variations in the sample.
In order to enhance the visibility of the structures within the low kV STEM images, a spectral bandpass filter was applied utilizing a first-order Butterworth bandpass filter to suppress filtering artefacts. The cutoff frequencies (8 nm and 80 nm) of the filter were chosen to achieve optimum contrast for the whiskers in the filtered images thereby excluding large-scale contributions and noise without changing any structural information in the length scale of interest. After filtering and reverse transformation of the Fourier transform into an image and contrast optimization in figures 2e-h, the whiskers appear more prominent.
As the whiskers (STEM intensity changes) can originate from either local sample thickness variations or material domains with different density and atomic number within the bulk we performed AFM investigations of the sample surfaces. **Figure 6** shows an AFM image of an annealed active layer deposited at T = 90°C. The sample surface exhibits thickness variations in the

range of 5 nm and does not show any distinct structural features that can be correlated with the needle-like structures in the low-keV STEM images in **figure 4**.

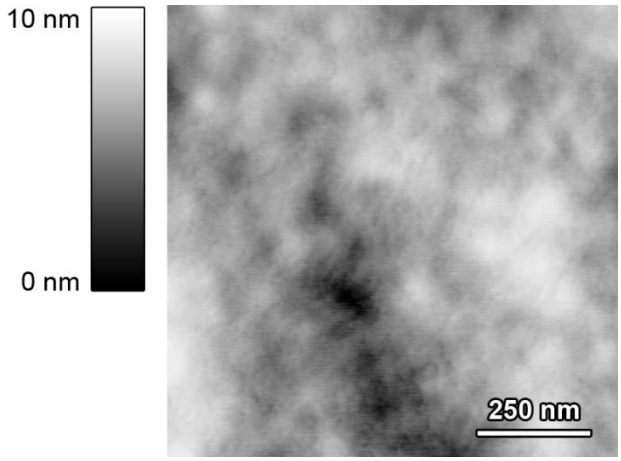

Figure 6. *Atomic force microscope surface image of a annealed P3HS:PCBM sample deposited at T = 90 °C.*
No needle-like structures are visible on the very smooth sample surface with feature heights in the range of 5 nm.

Hence the high image intensity of the needles can be correlated with a local increase of the atomic number and density. This is expected for P3HS domains because P3HS contains selenium and exhibits a higher average atomic number than PCBM (Z_{P3HS}= 7.27, Z_{PCBM} = 5.57). As Rutherford cross-sections are proportional to Z^2 and the cross-sections of different elements are additive, the average Z is the weighted root-mean-square of the atomic numbers of the constituent elements. As a result the large-angle electron scattering probability into the hollow cone is larger for P3HS as compared to PCBM. Due to the structural investigations in this work, the molecular affinity of P3HS to P3HT for which the formation of whiskers has already been reported [22], and the known tendency of P3HS to self-organize [23], we can attribute the needle-like structures to an enhanced π-π stacking and the subsequent formation of crystallites.
We further substantiated this finding by rinsing a thermally annealed sample with 1,8-octanedithiol (ODT) which selectively dissolves PCBM [24]. After a rinsing time of 10 s, the remaining ODT was removed in a nitrogen gas stream. **Figure 7a** shows a STEM micrograph of an annealed sample that was rinsed with ODT. Although the whiskers are notably superimposed by thickness variations from material agglomeration and suffer from a missing Z-contrast due to the absence of PCBM, the needle-like domain structures are still apparent. However, by applying bandpass filters between 8 and 80 nm we were able to make these whisker structures more distinguishable as depicted in **figure 7b**.

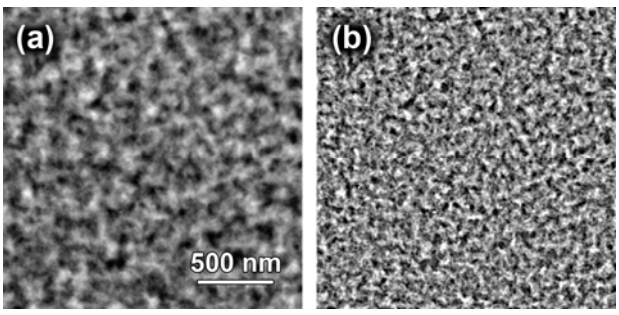

Figure 7. *Contrast enhanced, low-keV HAADF STEM (15 keV) images of peeled-off 2 µm × 2 µm P3HS:PCBM layer (T = 100 °C) after thermal post-treatment from which the PCBM was removed by rinsing the specimen with ODT: (a) The whiskers are still visible after removing PCBM. (b) First order Butterworth bandpass (8-80 nm) filtered image.*

4. Optoelectronic properties of P3HS:PCBM solar cells

The observations of changes in the P3HS:PCBM nano-morphology in conjunction with the formation of P3HS needle-like structures have a considerable impact on the optoelectronic properties of the respective photovoltaic devices.
The JV characteristics and key parameters of the as-prepared P3HS:PCBM solar cells show only a slight variation depending on the substrate/solution temperature T according to **table 1**.

Table 1. Solar cell key parameters.

Deposition Temperature	T	70 °C	80 °C	90 °C	100 °C
			Unannealed Devices		
Open circuit voltage	V_{OC}	0.68 V	0.74 V	0.71 V	0.67 V
Short circuit current density	J_{SC}	1.3 mA/cm^2	1.2 mA/cm^2	1.0 mA/cm^2	1.2 mA/cm^2
Fill factor	FF	35 %	34 %	33 %	33 %
Efficiency	H	0.3 %	0.3 %	0.2 %	0.3 %
			Annealed Devices		
Open circuit voltage	V_{OC}	0.52 V	0.52 V	0.51 V	0.51 V
Short circuit current density	J_{SC}	4.3 mA/cm^2	3.9 mA/cm^2	4.7 mA/cm^2	4.5 mA/cm^2
Fill factor	FF	54 %	50 %	60 %	59 %
Efficiency	H	1.2 %	1.0 %	1.4 %	1.4 %
Thickness		92 nm	65 nm	142 nm	82 nm

The open circuit voltage of all devices was in the order of V_{OC} = 0.7 V, the power conversion efficiency was about η = 0.3 % and the device short circuit current density was close to J_{SC} = 1.1 mA/cm^2 for all devices. **Figure 8** exemplifies the respective JV curve of a sample processed at T = 90 °C.

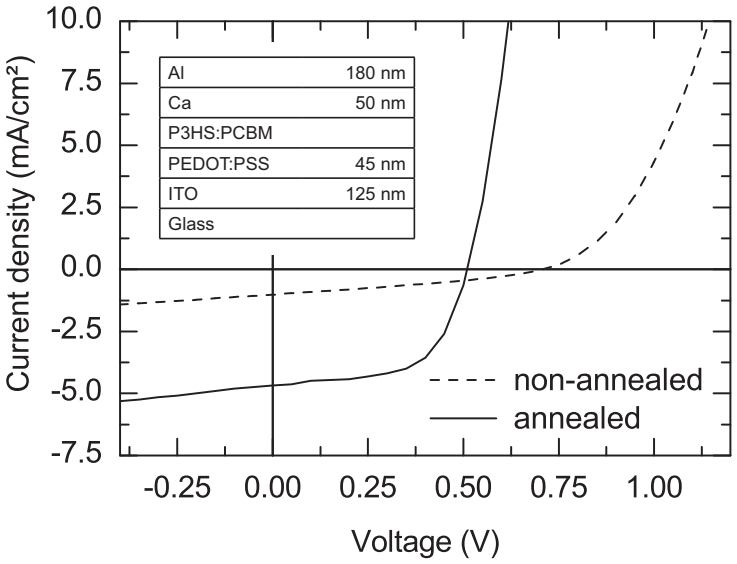

Figure 8. *JV curves of ITO/PEDOT:PSS/P3HS:PCBM/Ca/Al solar cells (inset) under illumination at 92 mW/cm^2. The P3HS:PCBM chlorobenzene solution was spincast at T = 90 °C. Thermal annealing (150 °C, 6 min) strongly improved the performance of the OSCs.*

After measuring the cell performance of the solar cells as deposited we thermally annealed and characterized the samples again. As shown in figure 6 and table 1, V_{OC} was reduced, but J_{SC} and FF simultaneously improved significantly and consequently led to an increase in power conversion efficiency of up to η = 1.4 %. We note that the fill factor after annealing is correlated to the active's layer thickness.
During annealing we observed a change of the active layer's color indicating a change in absorption. As shown in **figure 9**, a shoulder appears in the absorption spectrum of the annealed devices at 680 nm. At the same time the maximum of the π-π*-absorption peak is shifted from 510

nm to 570 nm. No significant change is detected at wavelengths below 400 nm as the absorption in this wavelength region is dominated by the absorption of PCBM.

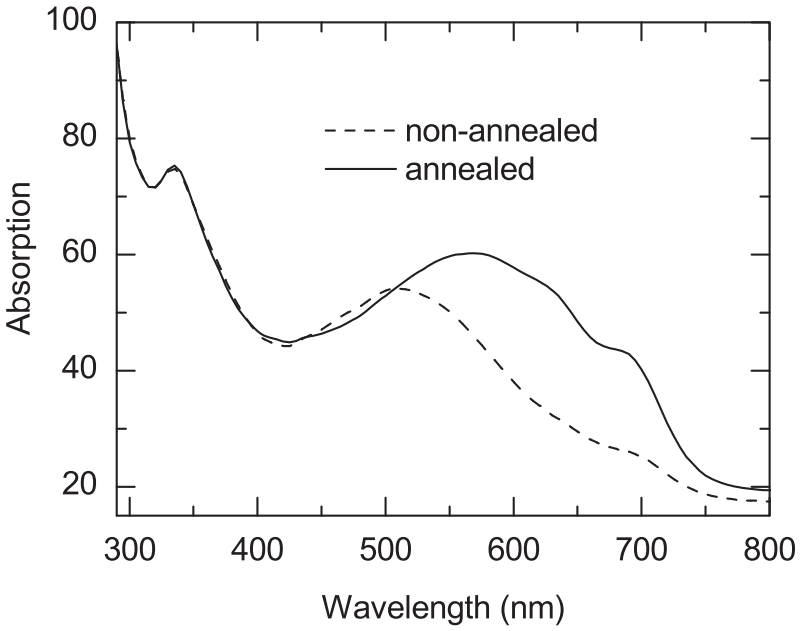

Figure 9. *Annealing of the P3HS:PCBM active layers leads to a significant enhancement of the red and near-infrared device absorption.*

Elevated temperatures enable the diffusion and aggregation of PCBM and a subsequent rearrangement of P3HS in the PCBM free regions similar to P3HT:PCBM blends [25]. The number of structural defects like chain kinks in P3HT is reduced upon annealing leading to an increase of the mean conjugation length [26]. This might explain the red-shift of the π-π^* absorption maximum. Additionally, the polymer crystallizes and forms lamellae [9] accounting for the strong vibronic shoulder at 680 nm being in accordance with prior observations [23]. The absorption is increased towards lower photon energies and subsequently the spectral coverage of the solar spectrum is increased. More photons are harvested leading to an increased current density as compared to the non-annealed devices.

Besides an improved photon harvesting through a broader absorption, the significant increase of the device short circuit current density can be attributed to improved transport paths for the charge carriers through the active layer due to the observed P3HS and PCBM aggregation. As the molecules form needle-like structures one can also expect a higher charge carrier mobility within the active layer. We have performed time-resolved photoresponse measurements in order to compare the charge carrier mobility within the active layer before and after thermal annealing utilizing a device architecture as depicted in **figure 10** (inset).

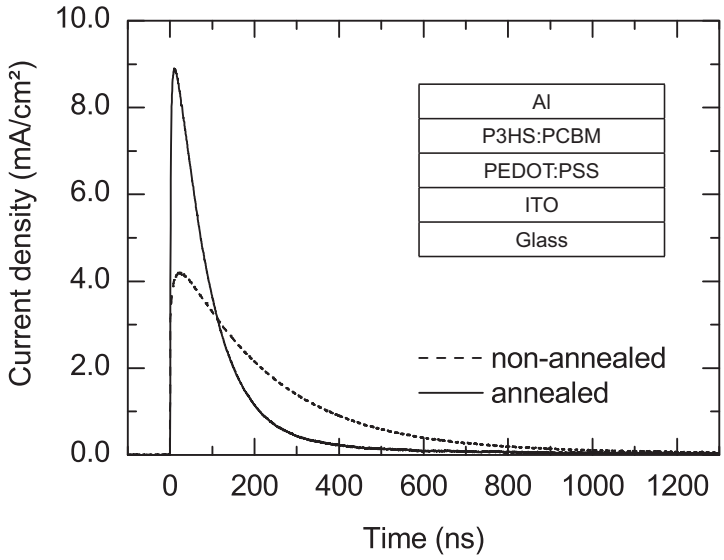

***Figure 10**. Time-resolved photo response of small OSCs. A bias voltage of V_{Bias} = -3 V was applied. Inset: The device architecture comprises a P3HS:PCBM absorbing layer embedded between an aluminum cathode and an PEDOT:PSS/ITO anode.*

The time-dependent photo response after laser excitation in **figure 10** shows a faster decline in current density of the annealed devices compared to pristine devices. During the measurement a constant negative bias voltage V_{Bias} = -3 V was applied to the device in order to accelerate the extraction of the photo-generated charge carriers. As discussed by Christ et al. [F1.2:3] a more pronounced peak and a faster decay in current density can be directly attributed to a higher charge carrier mobility and thus a more efficient charge carrier extraction from the device leading to an enhanced short circuit current density.

5. Conclusion

The nano-morphology of bulk heterojunctions comprising P3HS and PCBM was studied by means of low-energy HAADF STEM and correlated with the optoelectronic properties of respective organic solar cells. The morphological studies were performed on the very same devices that were characterized with respect to optoelectronic properties before.

By utilizing low-keV HAADF STEM we were able to distinguish between P3HS and PCBM domains in the active layers of organic photovoltaic devices. Upon thermal annealing we observe the formation of needle-like P3HS domains (whiskers) within the P3HS:PCBM blend and a shift of the predominant structure sizes towards 30 nm as derived from the isotropic representation of the 2D-DFT of the respective STEM images. We attribute the formation of P3HS whiskers to P3HS self-organization in connection with improved π-π stacking leading to the formation of crystallites. The absorption of photons with lower energies and the charge carrier mobilities are enhanced resulting in an increased current density and fill factor of the organic solar cells. Consequently, the power conversion efficiencies are improved up to about five times.

Our investigations demonstrate that HAADF STEM at low electron energies is well suited to obtain sensitive Z-contrast of carbon-based materials with only small atomic number difference. Knock-on damage can be avoided almost completely. Moreover, images can be taken in a conventional scanning electron microscope equipped with a STEM detector which is available in many laboratories.

References

- own work with complete titles -

[F1.2:3] N. S. Christ, S. W. Kettlitz, S. Valouch, S. Züfle, C. Gärtner, M. Punke, U. Lemmer, Nanosecond Response of Organic Solar Cells and Photodetectors, *J. Appl. Phys.* **2009**, *105*, 104513.

[F1.2 :7] B. Schmidt-Hansberg, M.F.G. Klein, K. Peters, F. Buss, J. Pfeifer, S. Walheim, A. Colsmann, U. Lemmer, P. Scharfer, W. Schabel, In situ monitoring the drying kinetics of knife coated polymer-fullerene films for organic solar cells, *J. Appl. Phys.* **2009**, *106*, 124501.

[F1.2:11] M. Pfaff, E. Müller, M.F.G. Klein, A. Colsmann, U. Lemmer, V. Krzyzanek, R. Reichelt, D. Gerthsen, Low-energy electron scattering in carbon-based materials analyzed by scanning transmission electron microscopy and its application to sample thickness determination, *Journal of Microscopy* **2010**, DOI: 10.1111/j.1365-2818.2010.03475.x

[1] G. Yu, J. Gao, J. C. Hummelen, F. Wudi, A. J. Heeger, *Science* **1995**, *270*, 1789-1791.

[2] M. Heeney, W. Zhang, D. J. Crouch, M. L. Chabinyc, S. Gordeyev, R. Hamilton, S. J. Higgins, I. McCulloch, P. J. Skabara, D. Sparrowea, S. Tierney, *Chem. Commun.* **2007**, *47*, 5061-5063.

[3] NREL, Certificate Solarmer, 7.9 % under AM1.5 spectrum **2009**.

[4] S. H. Park, A. Roy, S. Beaupré, S. Cho, N. Coates, J. S. Moon, D. Moses, M. Leclerc, K. Lee, Alan J. Heeger, *Nat. Photonics* **2009**, *3*, 297.

[5] A. Haugeneder, M. Neges, C. Kallinger, W. Spirkl, U. Lemmer, J. Feldmann, U. Scherf, E. Harth, A. Gügel, K. Müllen, *Phys. Rev. B.* **1999**, *59,* 15346-15351.

[6] C. Brabec, V. Dyakonov, U. Scherf , in *Organic Photovoltaics: Materials, Device Physics, and Manufacturing Technologies*, Wiley-VCH, Weinheim, Germany **2008**.

[7] A. J. Moulé, K. Meerholz, *Adv. Funct. Mater.* **2009**, *19*, 1-9.

[8] J. Peet, J. Y. Kim, N. E. Coates, W. L. Ma, D. Moses, A. J. Heeger, G. C. Bazan, *Nat. Materials* **2007**, *6*, 497-500.

[9] W. Ma, C. Yang, X. Gong, K. Lee, A. J. Heeger, *Adv. Funct. Mater.* **2005**, *15,* 1617-1622.

[10] G. Li, V. Shrotriya, Y. Yao, Y. Yang, *J. Appl. Phys.* **2005**, *98*, 043704.

[11] V. Shrotriya, Y. Y., G. Li, Y. Yang, *Appl. Phys. Lett.* **2006**, *89*, 063505.

[12] F. Banhart, *Rep. Prog. Phys.* **1999**, *62*, 1181-1221.

[13] A. Howie, *J. Microsc.* **1979**, *117*, 11-23.

[14] S. J. Pennycook, L. A. Boatner, *Nature* **1988**, 336, 565-567

[15] P. Hartel, H. Rose, C. Dinges, *Ultramicroscopy* **1996**, 63, 93-114

[16] V. Borries, E. Ruska, *Zeitschrift für Physik A Hadrons and Nuclei* **1940**, 116, 249-256

[17] A. Delong, K. Hladil, V. Kolařík, P. Pavelka, *EUREM 12 conference paper*, Vol. III, **2000**, 197

[18] V. E. Cosslett, R. N. Thomas, *British Journal of Applied Physics* **1964**, 15, 883-907

[19] W. Bothe, *Handbuch der Physik 22,2: Negative und positive Strahlen*, 2nd edition, Springer, **1933**, 1-74.

[20] C. Deumié, R. Richier, P. Dumas, C. Amra, Appl. Opt. 1996, 35, 5583-5594.

[21] S.J. Fang, S. Haplepete, W. Chen, C. R. Helms, *J. Appl. Phys.* **1997**, *82*, 5891.

[22] K. J. Ihn, J. Moulton, P. Smith, *J. Polym. Sci. Part B: Polym. Phys.* **1993**, *31*, 735-742.

[23] A. M. Ballantyne, L. Chen, J. Nelson, D. D. C. Bradley, Y. Astuti, A. Maurano, C. G. Shuttle, J. R. Durrant, M. Heeney, W. Duffy, I. McCulloch, *Adv. Mater.* **2007**, *19*, 4544-4547.

[24] J. K. Lee, W. L. Ma, C. J. Brabec, J. Yuen, J. S. Moon, J. Y. Kim, K. Lee, G. C. Bazan, A. J. Heeger, *J. Am. Chem. Soc.* **2008**, *130*, 3619-3623.

[25] M. Campoy-Quiles, T. Ferenczi, T. Agostinelli, P. G. Etchegoin, Y. Kim, T. D. Anthopoulos, P. N. Stavrinou, D. D. C. Bradley, J. Nelson, *Nat. Materials* **2008**, *7*, 158-164.

[26] U. Zhokhavets, T. Erb, G. Gobsch, M. Al-Ibrahim, O. Ambacher, *Chem. Phys. Lett.* **2006**, *418*, 347-350.